Al^{3+}-substituted nanocrystalline Cu$_{0.5}$Zn$_{0.5}$Al$_x$Fe$_{2-x}$O$_4$ spinel ferrite onto the rGO sheets as green photocatalyst nano-heterostructured materials

Aqsa Riaz[a], Rasheda Bibi[a], Sobia Jabeen[b], Sonia Zulfiqar[c], Philips O. Agboola[d],
Imran Shakir[e], Muhammad Farooq Warsi[a,*]

[a]*Department of Chemistry, Baghdad-ul-Jadeed Campus, The Islamia University of Bahawalpur, Bahawalpur-63100, Pakistan,
Tel. +92 62 9255473; emails: farooq.warsi@iub.edu.pk (M.F. Warsi), aqsariaz886@yahoo.com (A. Riaz), rasheda.meer@yahoo.com (R. Bibi)*
[b]*Department of Physics, Quaid-i-Azam University Islamabad-45320, Pakistan, email: sobia.atif.ch@gmail.com (S. Jabeen)*
[c]*Department of Chemistry, School of Sciences and Engineering, The American University in Cairo, New Cairo, 11835 Egypt,
email: sonia.zulfiqar@aucegypt.edu (S. Zulfiqar)*
[d]*College of Engineering Al-Muzahmia Branch, King Saud University, P.O. Box: 800, Riyadh 11421, Saudi Arabia,
email: paboola@ksu.edu.sa (P.O. Agboola)*
[e]*Sustainable Energy Technologies Center, College of Engineering, King Saud University, P.O. Box: 800, Riyadh 11421,
Saudi Arabia, email: mshakir@ksu.edu.sa (I. Shakir)*

ABSTRACT

Synthesis of magnetically separable Cu$_{0.5}$Zn$_{0.5}$Al$_x$Fe$_{2-x}$O$_4$ nanoparticles was carried out via a chemical co-precipitation route. The synthesis of Cu$_{0.5}$Zn$_{0.5}$Al$_x$Fe$_{2-x}$O$_4$-rGO nano-heterostructures was done by the ultrasonication method. Cu$_{0.5}$Zn$_{0.5}$Al$_x$Fe$_{2-x}$O$_4$ nanoparticles were characterized by X-ray diffraction (XRD). XRD analysis confirmed the cubic spinel structure of Cu$_{0.5}$Zn$_{0.5}$Fe$_2$O$_4$ nanoparticles and its derivatives (Cu$_{0.5}$Zn$_{0.5}$Al$_x$Fe$_{2-x}$O$_4$, where x = 0.00, 0.03, 0.06, 0.09, 0.12, and 0.15). The substitution of Fe^{3+} ions with Al^{3+} ions was confirmed by peak shifting in recorded XRD patterns. Further, an ener-gy-*dispersive* X-ray analysis of all samples showed the variation in Fe^{3+} and Al^{3+} contents quantita-tively. The characterization of graphite oxide (GO) and reduced graphene oxide (rGO) was carried out via XRD, UV-visible (UV-Vis.), and Raman spectroscopy. The data of all these three techniques confirmed the formation of rGO and GO. The fully characterized rGO was then utilized for making nano-heterostructures with Cu$_{0.5}$Zn$_{0.5}$Al$_x$Fe$_{2-x}$O$_4$ nanoparticles. Scanning electron microscopy analysis confirmed the formation of ferrite nanoparticles-rGO nano-heterostructures. The Cu$_{0.5}$Zn$_{0.5}$Al$_x$Fe$_{2-x}$O$_4$ nanoparticles and Cu$_{0.5}$Zn$_{0.5}$Al$_x$Fe$_{2-x}$O$_4$-rGO nano-heterostructures were subjected to various types of characterizations for their potential applications. Electrochemical impedance spectroscopy revealed that the charge transfer resistance significantly reduced for nano-heterostructures as compared to bare Cu$_{0.5}$Zn$_{0.5}$Al$_{0.03}$Fe$_{1.97}$O$_4$ nanoparticles. The photocatalytic degradation efficiency of the prepared nanoparticles and their nano-heterostructures with rGO was carried out by monitoring the degra-dation of typical organic compound methylene blue (MB) using UV-Vis. spectroscopy. It is inter-esting to note that the photocatalytic activity of Cu$_{0.5}$Zn$_{0.5}$Al$_x$Fe$_{2-x}$O$_4$ photocatalyst was significantly increased when Cu$_{0.5}$Zn$_{0.5}$Al$_{0.03}$Fe$_{1.97}$O$_4$/rGO nanocomposites were used as a catalyst. This is because of rGO as it takes the light generated electron from the conduction band of catalyst immediately and thus inhibits the immediate recombination of e$^−$–h$^+$ pairs. Secondly, due to the large surface area of rGO sheets, several MB molecules could be adsorbed on its surface. The adsorbed molecules later on degraded by the photocatalytic reaction.

Keywords: Visible light; Photocatalysis; Ferrite; rGO; Nano-heterostructures

* Corresponding author.

1. Introduction

With the passage of time, contaminants in water are being increased to many folds which affect the quality of drinking water [1]. The effluent from the industries pollutes the drinking water and also has an adverse effect on human health. There are different types of impurities in wastewater, for example, organic-based compounds, inorganic metals ions, and pathogens. Filtration, coagulation, aeration, and boiler water treatment are some old methods that were being used in the past to clean the drinking water. However, these methods are not enough for the proper degradation of contaminants in wastewater.

Now a day several attempts are going on to degrade the organic contaminants completely from the wastewater. Photocatalysis plays a vital role in this regard and has a large scope over the old methods to get rid of organic-based impurities. The first reported photocatalyst was titania (TiO_2) in 1972 [2]. It has several advantages, due to which it was selected as a photocatalyst for the oxidative degradation of volatile organic components in the presence of UV irradiation [3]. For example, it has good chemical stability, less toxicity and is economically cheap material. However, it also has some major drawbacks that hampered its commercialization. First, it has a relatively large bandgap (3.2 eV). This large value of bandgap needs UV light for a generation of electron-hole pairs [4]. UV radiations comprises 3%–4% of sunlight and >40% of visible radiations [5]. Secondly, it cannot be easily separated from the reaction mixture [6]. Thus, it cannot be reused and recycled easily.

Therefore, interests have been developed to utilize those materials having maximum efficiency to absorb the visible light. To overcome this deficiency, several attempts are in progress to design such photocatalytic materials that have a small bandgap and corresponds to the visible light 400–800 nm [6–8]. Ferrites are magnetic materials with Fe as a major element and they already have accepted the challenge, which was not fulfilled by TiO_2. They absorb light in the visible region due to their smaller bandgap. For example, $ZnFe_2O_4$ with a bandgap of 1.9 eV is photo-catalytically active in the visible region [9]. Another advantage is the recovery of ferrites from the reaction mixture due to their magnetic property and due to which these can be reused and recycled easily [10]. Erbium-substituted $Ni_{0.4}Co_{0.6}Fe_2O_4$ ferrite nanoparticles were synthesized and analyzed for photocatalytic properties which can be used and recycled by applying a magnetic field around the reactor [11].

The magnetically separable photocatalyst is called green photocatalyst as it can be recovered at the end of reaction by applying a conventional external magnetic field. For example, MnO_2 sheets coated with Fe_2O_4 nanocomposite could be magnetically separated and reused [12]. It was observed that ferrites are poor conductors because when ferrites are alone used as a photocatalyst, these are not able to stop the recombination of photoexcited electron-hole pairs.

To overcome this problem, various strategies are being developed. For example, it has been reported in the literature that if rGO is mixed with ferrite nanoparticles, the rGO could capture the photoexcited electrons and thus prevent the recombination of electron-hole pairs. The rGO can provide transportation path for electrons and thus inhibits unwanted recombination of electron and hole pairs. Because of high catalytic activity, chemical stability and excellent conductivity, rGO provides support for photocatalyst by improving the surface area and conductivity of photocatalytic materials [13]. For example, $CoFe_2O_4$ alone is not active as photocatalyst in the visible region. However, when it is combined with rGO it shows excellent photocatalytic activity for methylene blue degradation [1]. $Ni_{0.65}Zn_{0.35}Fe_2O_4$ spinel ferrite nanoparticles were synthesized and photocatalytic degradation efficiency was analyzed. It was found that rGO based nano-hybrids exhibited maximum degradation efficiency [14]. Similarly, Zirconium substituted $Mg_{0.2}Co_{0.8}Fe_2O_4$ ferrite nanoparticles and their hybrids based on reduced graphene oxide (rGO) were also analyzed for photocatalytic degradation activity [15].

Graphene-based Er^{3+} substituted Cobalt-Zinc ferrites [16] nanoparticles were fabricated for photocatalytic degradation under visible light illumination. The degradation experiment showed significant enhancement in degradation efficiency while using graphene-based nanohybrid. Cobalt zinc ferrite nanorods were [17] reported for photocatalytic degradation of several pollutants. It was found that the fabricated nanorods exhibited up to 58% degradation under solar light exposure. Fan et al. [18] reported the successful synthesis of $Zn_{0.8}Co_{0.2}Fe_2O_4$ ferrite nanoparticles with smaller bandgap energy for photocatalytic degradation of both colored (methylene blue) and colorless (2,4,6-trichlorophenol and salicylic acid sodium) pollutant under the visible light source. The observed photoreduction up to 81% was noticed in the case of 2,4,6-trichlorophenol. Nickel zinc ferrite nanoparticles/ZnO nanocomposite [19] was synthesized by the hydrothermal method and applied for the photoreduction process. It was found that the synthesized nanocomposite degraded pollutants via the Z-scheme approach. Here in this article, we report the role of rGO to tailor the photocatalytic activity of $Cu_{0.5}Zn_{0.5}Al_{0.03}Fe_{1.97}O_4$ nanoparticles anchored onto the 2D rGO sheets.

2. Experimental work

Synthesis of $Cu_{0.5}Zn_{0.5}Al_xFe_{2-x}O_4$ nanoparticles was done using the co-precipitation route [20]. All chemicals of analytical grade were used as received. For a typical batch synthesis, the stoichiometric ratio of freshly prepared metal salts solutions in deionized water was mixed in different beakers. pH was elevated using the fresh ammonia solution. After the desired stirring, precipitates were neutralized by washing using deionized water to almost neutral pH. Ground precipitates were then annealed 800°C for 7 h. rGO was prepared in two steps that involved the oxidation of graphite powder into graphite oxide (GO) and then GO was reduced into rGO. A modified literature protocol was adopted for the synthesis of rGO [21]. Nano-heterostructures of rGO and $Ni_{0.65}Zn_{0.35}Fe_2O_4$ nanoparticles were prepared by using the sonication method. The mixture of $Ni_{0.65}Zn_{0.35}Fe_2O_4$ and rGO was prepared by adding 0.01 g of reduced graphite oxide and 0.09 g of $Ni_{0.65}Zn_{0.35}Fe_2O_4$ into 10 cm^3 of deionized water. The sample solution was sonicated for 1 h. After the sonication solution was dried in an oven at 100°C and then the sample was ground by using pestle and mortar.

The surface morphology of samples was investigated using ZEISS LEO SUPRA 55 field emission scanning electron

microscope and EDX analysis was carried out on JEOL JCM-6000 Plus SEM. All UV-Visible measurements were carried out on Cary-60 spectrophotometer. Electrochemical data was collected on PGZ-402 (Radiometer Analytical).

3. Results and discussion

UV-visible (UV-Vis.) spectra of both GO and rGO are shown in Fig. 1a. The UV-visible spectra of GO and rGO show that in the case of GO, the absorption peak occurs at 228 nm. This peak is referred to as л–л* transitions of aromatic C–C bonding while weak absorption observes at 288 nm. This absorption is due to *n–л** transitions of C=O bonds [22,23]. While in the case of rGO, the absorption peak observes at 253 nm due to the redshift after the reduction [23]. In rGO, due to reduction, the Sp^3 hybridized carbon atom changes into Sp^2 hybridized carbon atom indicating the increase in electronic conjugation and removal of functional groups [23].

UV-visible absorption spectra of the overall series are shown in Fig. 2. It was found that $Ni_{0.65}Zn_{0.35}Fe_2O_4$ nanomaterials show a sharp absorption band in the visible region at 536 nm. This visible-light absorption is responsible for its solar light response in the degradation experiment. Fig. 3 shows the bandgap energy of $Cu_{0.5}Zn_{0.5}Al_xFe_{2-x}O_4$ nanoparticle and from Fig. 3 it was noted that $Cu_{0.5}Zn_{0.5}Al_{0.03}Fe_{1.97}O_4$ nanoparticles exhibited the lowest bandgap (2.02 eV) energy.

The X-ray diffraction (XRD) spectra of rGO and GO are shown in Fig. 1b. In this spectra, GO shows a broad peak at $2\theta = 10.9°$. This corresponds to the (001) reflection plane with an average interlayer spacing of 0.808 nm. This spacing is much greater than natural graphite (0.35 nm) due to the intrusion of oxygen-containing functional groups in the flacks of graphite oxide. Therefore, it is confirmed that graphite has been transformed completely into graphite oxide. On the other hand, a high-intensity sharp peak observes at an angle of $2\theta = 25°$ which corresponds to (002) reflection plane which proved the formation of rGO. Interlayer spacing of rGO was calculated (0.396 nm) which is less than that of GO due to the removal of water molecules and oxygenated functional groups. This smaller interlayer spacing of rGO shows that graphite oxide has been exfoliated and rGO is prepared [24].

Raman analysis is a potential technique employed to depict structural as well as vibrational characteristics of synthesized materials. Raman spectra of graphite, GO, and rGO are shown in Fig. 4. The D and G bands are present in Raman spectra of Graphite, GO, and rGO. However, the intensity corresponding to D and G bands is much different. In the case of Graphite, D and E bands have appeared at 1,337 and 1,564 cm^{-1}, respectively. Whereas in the case of GO, the D and E bands appeared at 1,343$^-$ and 1,586 cm^{-1}, respectively. The D band is responsible due to sp^3 carbon atoms. However, the G band has corresponded to in-plane vibrations of sp^2 carbons. The D/G ratio for Graphite, GO and rGO was found to be 0.25, 0.97, and 1.00, respectively. This increase in the D/G ratio confirmed the formation of rGO sheets from GO [15].

The crystalline structure of synthesized $Cu_{0.5}Zn_{0.5}Al_xFe_{2-x}O_4$ nanoparticles with different concentrations of aluminum as a dopant was carried out with the help of XRD [25]. Fig. 5a showed the diffraction peaks of $Cu_{0.5}Zn_{0.5}Al_xFe_{2-x}O_4$ nanoparticles at 2θ values of [30°, 34.5°, 35.89°, 41°, 43.46°, 49.94°,54.35°, 64.45°, 65.5°] from Brag's planes of diffraction [220, 211, 311, 222, 400, 422, 511, 440, 103] with the peak of highest intensity [311] at an angle of 35.89°. This matches very well with the literature value for spinel crystal of zinc ferrites [JCPDS card No. 82-1049] [26]. XRD pattern of ferrite/composite did not show any peak of rGO. It has been reported in the literature, that quite often metal oxide/graphene XRD pattern did not show any peak of rGO [27].

Cell software was used to calculate cell constants for different composition that lies in the limits of [8.30–8.36 Å] [28]. The average cell volume of $Cu_{0.5}Zn_{0.5}Al_xFe_{2-x}O_4$ nanoparticles was about 573 nm^3. Crystallite size of $Cu_{0.5}Zn_{0.5}Al_xFe_{2-x}O_4$ nanoparticles was calculated using Debye-Scherrer's equation which is $D = K\Lambda/\beta Cos\theta$ (Eq. (1)).

In this equation, the K is form factor with a number value of 0.9 and β is the average value of maximum width of highest intensity peak at half of its intensity (FWHM), Λ is the wavelength of radiations used that is 1.54 Å, θ is the diffraction angle. The crystallite size of these $Cu_{0.5}Zn_{0.5}Al_xFe_{2-x}O_4$ nanoparticles was observed in the range of 28–50 nm. The irregular trend in the crystallite size of particles was observed with the increasing Al^{3+} contents. The reason is that the ionic
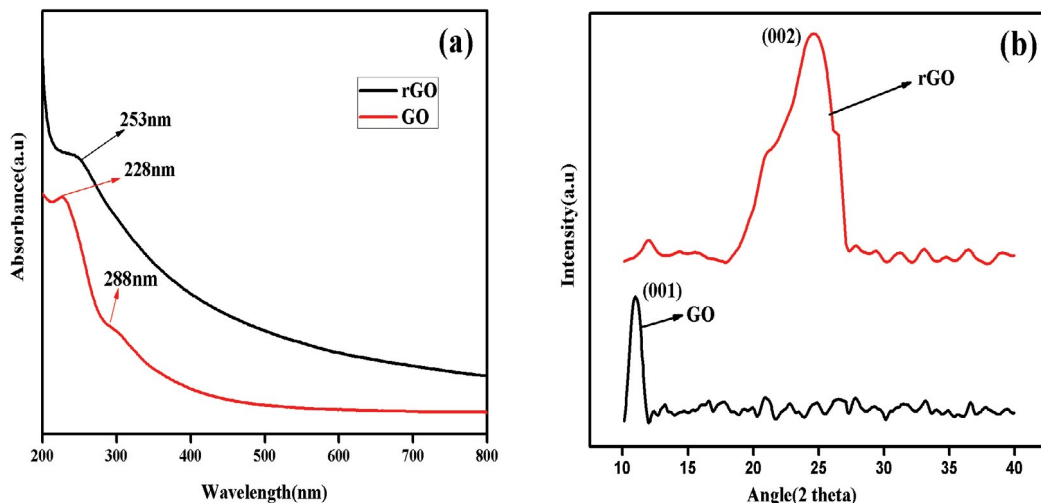

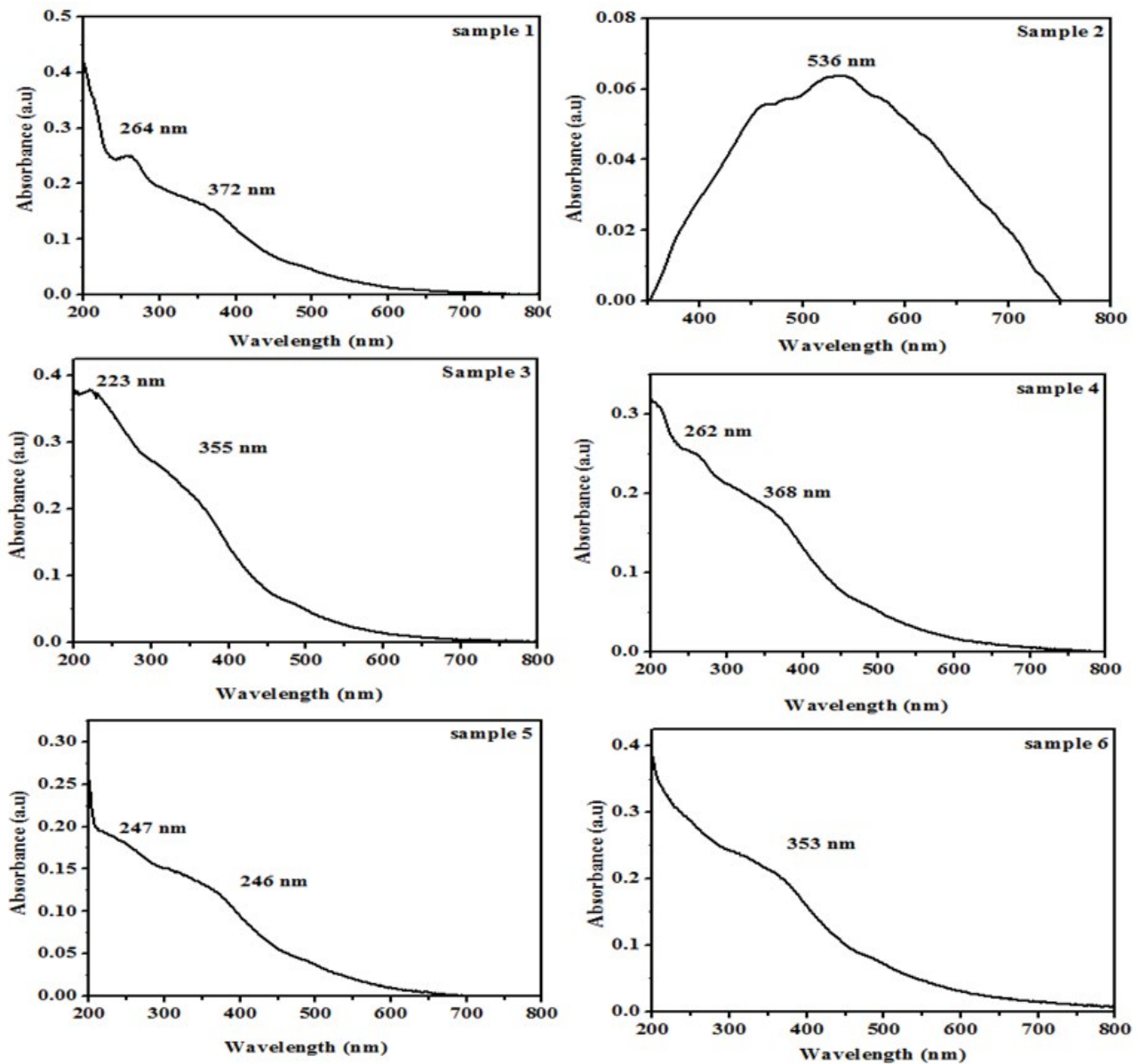Fig. 1. (a) UV-Visible spectra of GO and rGO and (b) XRD spectra of GO and rGO.

Fig. 2. UV-visible spectra of $Cu_{0.5}Zn_{0.5}Al_xFe_{2-x}O_4$ nanoparticles.

radius of dopant Al^{+3} ion is 0.053 nm while the ionic radius of replaced species Fe^{+3} is 0.060 nm, so when Fe^{+3} is replaced by Al^{+3} then the size of synthesized $Cu_{0.5}Zn_{0.5}Al_xFe_{2-x}O_4$ particles is slightly decreased [29]. The following equations were used to calculate X-ray density, bulk density, and porosity of $Cu_{0.5}Zn_{0.5}Al_xFe_{2-x}O_4$ nanoparticles [30].

$$Bulk\ density\ (\rho_{bulk})\ of\ Cu_{0.5}Zn_{0.5}Al_xFe_{2-x}O_4\ nanoparticles = m/V \tag{1}$$

Here "m" and "V" are the mass and volume of the pallet respectively which is calculated by using formula $V = 4\pi l^2 d$ while "d" and "l" are the thickness and radius of the pallet.

$$X\text{-ray density }_{(\rho_{x\text{-ray}})}\ Cu_{0.5}Zn_{0.5}Al_xFe_{2-x}O_4\ nanoparticles = 8M/N_AV \tag{2}$$

Here in Eq. (2) "M" is the molecular weight of the $Cu_{0.5}Zn_{0.5}Al_xFe_{2-x}O_4$ nanoparticles composition, "N_A" is Avogadro number, "V" is the cell volume.

$$Porosity\ of\ Cu_{0.5}Zn_{0.5}Al_xFe_{2-x}O_4\ nanoparticles = 1 - \rho_{bulk}/\rho_{x\text{-ray}} \tag{3}$$

The values of cell parameters and porosity are given in Table 1. X-ray density is greater than that of bulk density. The substitution of Fe^{3+} ions with Al^{3+} ions was confirmed by peak shifting toward a higher angle as given in Fig. 5b.
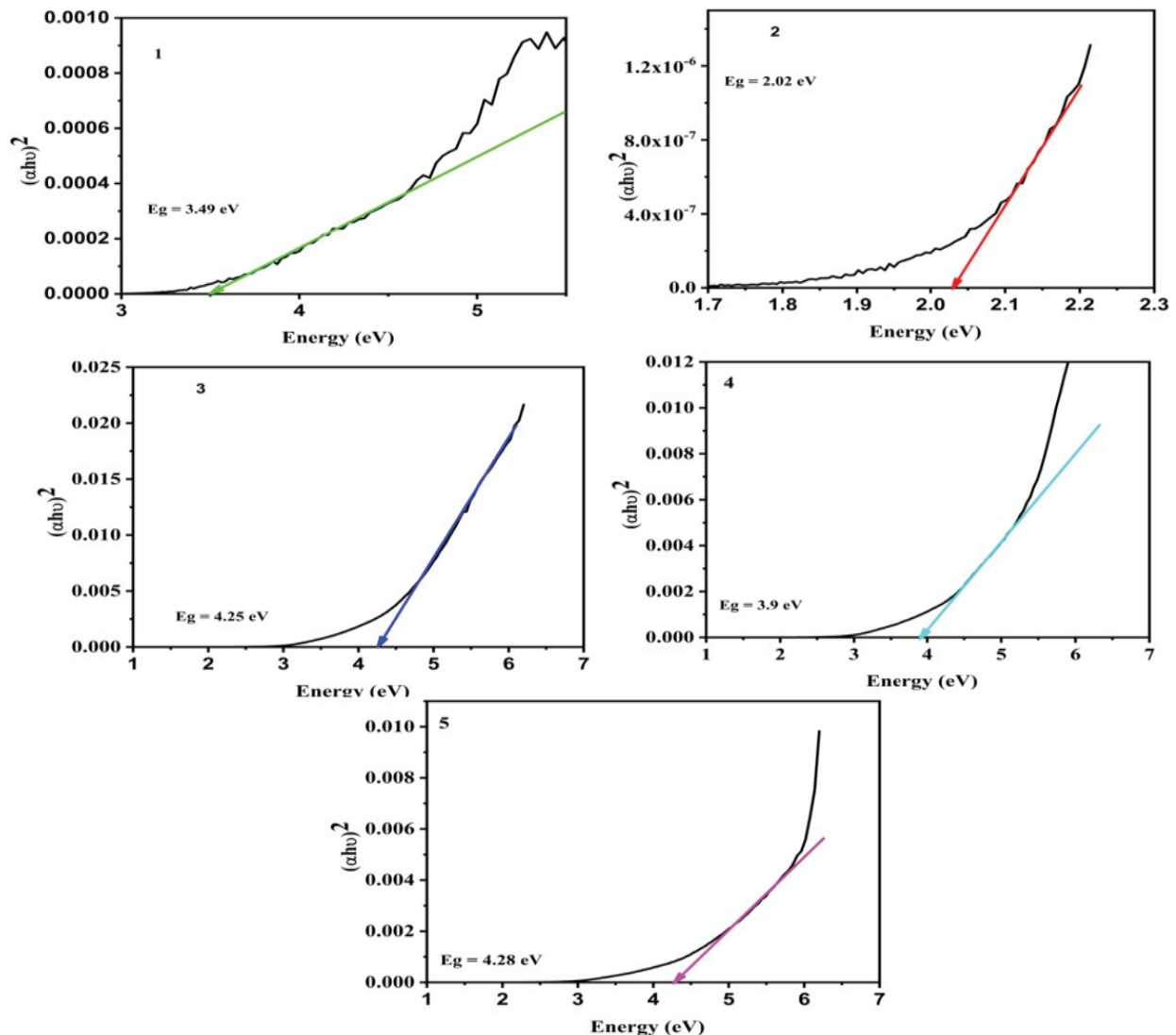
Fig. 3. (1–5) Bandgap energies of $Cu_{0.5}Zn_{0.5}Al_xFe_{2-x}O_4$ nanoparticles.

Scanning electron microscopy (SEM) is used to study the information about particle size of $Cu_{0.5}Zn_{0.5}Al_xFe_{2-x}O_4$ nanoparticles and to confirm the formation of nano-hetero-structures of $Cu_{0.5}Zn_{0.5}Al_xFe_{2-x}O_4$-rGO. The particle size of $Cu_{0.5}Zn_{0.5}Al_xFe_{2-x}O_4$ nanoparticles was about ~100 nm. The SEM image of $Cu_{0.5}Zn_{0.5}Al_xFe_{2-x}O_4$-rGO is shown in Fig. 6. It is clearly shown from the SEM image that $Cu_{0.5}Zn_{0.5}Al_xFe_{2-x}O_4$ nanoparticles finally dispersed among the layers of rGO. Further, the energy-dispersive X-ray (EDX) analysis of all samples was also carried out. The EDX data showed the variation in Fe^{3+} and Al^{3+} contents throughout the series. EDX results confirmed the successful substitution of Fe^{3+} ions with Al^{3+} ions and supported the XRD results.

Electrochemical impedance spectroscopy (EIS) is a more sensitive and non-destructive technique that is used to determine the charge transfer resistance of $Cu_{0.5}Zn_{0.5}Al_{0.03}Fe_{1.97}O_4$ and $Cu_{0.5}Zn_{0.5}Al_{0.03}Fe_{1.97}O_4$/rGO nanocomposites [1,31]. It is effectively used to determine the charge transfer resistance of $Ni_{0.65}Zn_{0.35}Fe_2O_4$ and $Ni_{0.65}Zn_{0.35}Fe_2O_4$/rGO nanocomposites.

With the help of this technique, the conducting materials on the electrode surfaces can be modified to get desirable capacitance and electrical resistance [32]. The Nyquist plot in Fig. 7 shows that the semicircle diameter of $Ni_{0.65}Zn_{0.35}Fe_2O_4$ is large as compared to the semicircle diameter of $Ni_{0.65}Zn_{0.35}Fe_2O_4$/rGO nanocomposites [1]. Smaller semicircle diameter means that the $Ni_{0.65}Zn_{0.35}Fe_2O_4$/rGO nanocomposites have smaller charge transfer resistance than that of $Ni_{0.65}Zn_{0.35}Fe_2O_4$. It is the two-dimensional structure of rGO that allows maximum charge transfer rate and lower the charge transfer resistance of $Ni_{0.65}Zn_{0.35}Fe_2O_4$/rGO nanocomposites. Due to the greater capability of charge transfer rate and because of lower charge transfer resistance of $Ni_{0.65}Zn_{0.35}Fe_2O_4$/rGO nanocomposites, these can be considered as best candidates for the photocatalytic activity.

Photogenerated electrons of $Ni_{0.65}Zn_{0.35}Fe_2O_4$/rGO trapped within the rGO sheets which lowered the of e^-–h^+ pairs recombination because of smaller charge transfer resistance of $Ni_{0.65}Zn_{0.35}Fe_2O_4$/rGO nanocomposites, the products

are expected to have large scale applications in supercapacitors, batteries, and other electrical appliances or power systems [33].

Photocatalysis is a versatile phenomenon that is used to remove contaminants from the water, air, and soil [34]. A lot

Fig. 4. Raman spectra of graphite, graphite oxide, and reduced graphene oxide.

of work on photocatalysis has been going on these days as it involves the conversion of toxic materials from our environment to less toxic ones such as water, CO_2, NH_4^+, NO_3^{-1}, Cl^{-1}, and SO_4^{-2}, etc. The photocatalytic reactions are initiated by light energy and in the present case, sunlight was used. For this purpose $Cu_{0.5}Zn_{0.5}Al_{0.03}Fe_{1.97}O_4$ nanoparticles and its rGO based composite were used as photocatalysts. This composition was chosen due to its lower bandgap energy. This lower bandgap energy is responsible for its solar light response. The light energy exposed to photocatalyst is responsible for the excitation of valance electrons to the conduction band. This causes the formation of holes in the valance band, thus electron-hole pairs will form [34]. These photogenerated e-h+ pairs are liable for oxidation-reduction reactions to occur. During the photocatalytic reaction, H_2O and hydroxyl (OH^-) react with hole and form $OH^•$ radicals. This generated $OH^•$ radical behaves as a primary oxidant. The generation of $OH^•$ radical takes place in two steps. T First step is the oxidation of OH^- ions and the second step is from dissolved O_2 in water reduced to $O_2^{•-}$ that further reacts with hole and form $^•OOH$ radical that decomposed into $OH^•$ radicals. The h+VB and e-CB are the best oxidizing and reducing agents [34,35]. It was observed that the photocatalytic activity of $Ni_{0.65}Zn_{0.35}Fe_2O_4$ nanoparticles was not much appreciated and can be enhanced by making its composites with $Ni_{0.65}Zn_{0.35}Fe_2O_4$/rGO nanocomposites proved to be the best
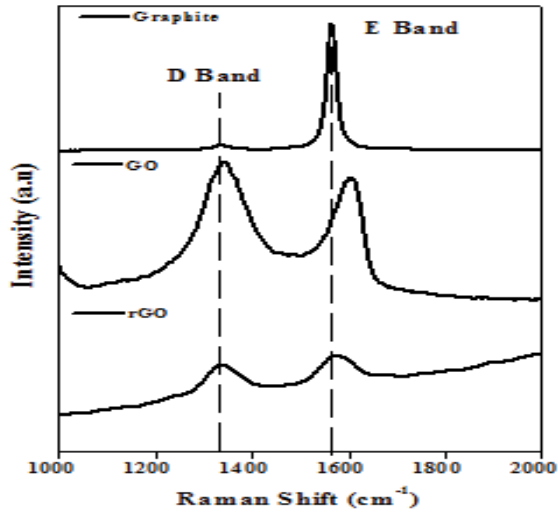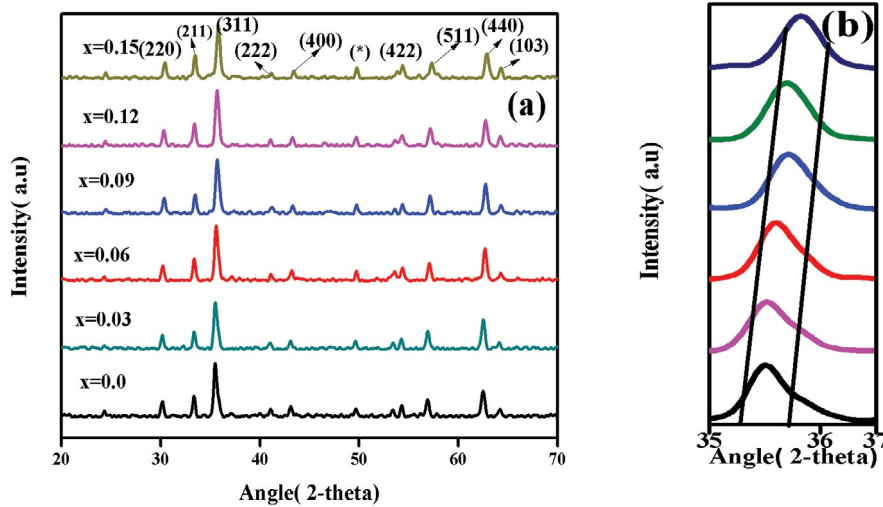

Fig. 5. (a) XRD spectra of $Cu_{0.5}Zn_{0.5}Al_xFe_{2-x}O_4$ nanoparticles and (b) peak shifting as a result of doping.

Table 1
Various cell and other physical parameters of $Cu_{0.5}Zn_{0.5}Al_xFe_{2-x}O_4$ nanoparticles

Sample	Cell length (Å)	Cell volume (Å³)	Bulk density (g/cm³)	X-ray density (g/cm³)	Porosity	Particle size (nm)
1	8.325	576.96	3.18	5.514	0.252	37.049
2	8.3061	573.04	3.205	5.491	0.285	31.091
3	8.3148	574.85	3.18	5.479	0.320	35.91
4	8.335	579.05	3.18	5.456	0.321	38.52
5	8.341	580.3	3.17	5.439	0.300	31.00
6	8.3628	584.86	3.175	5.419	0.29	28.12
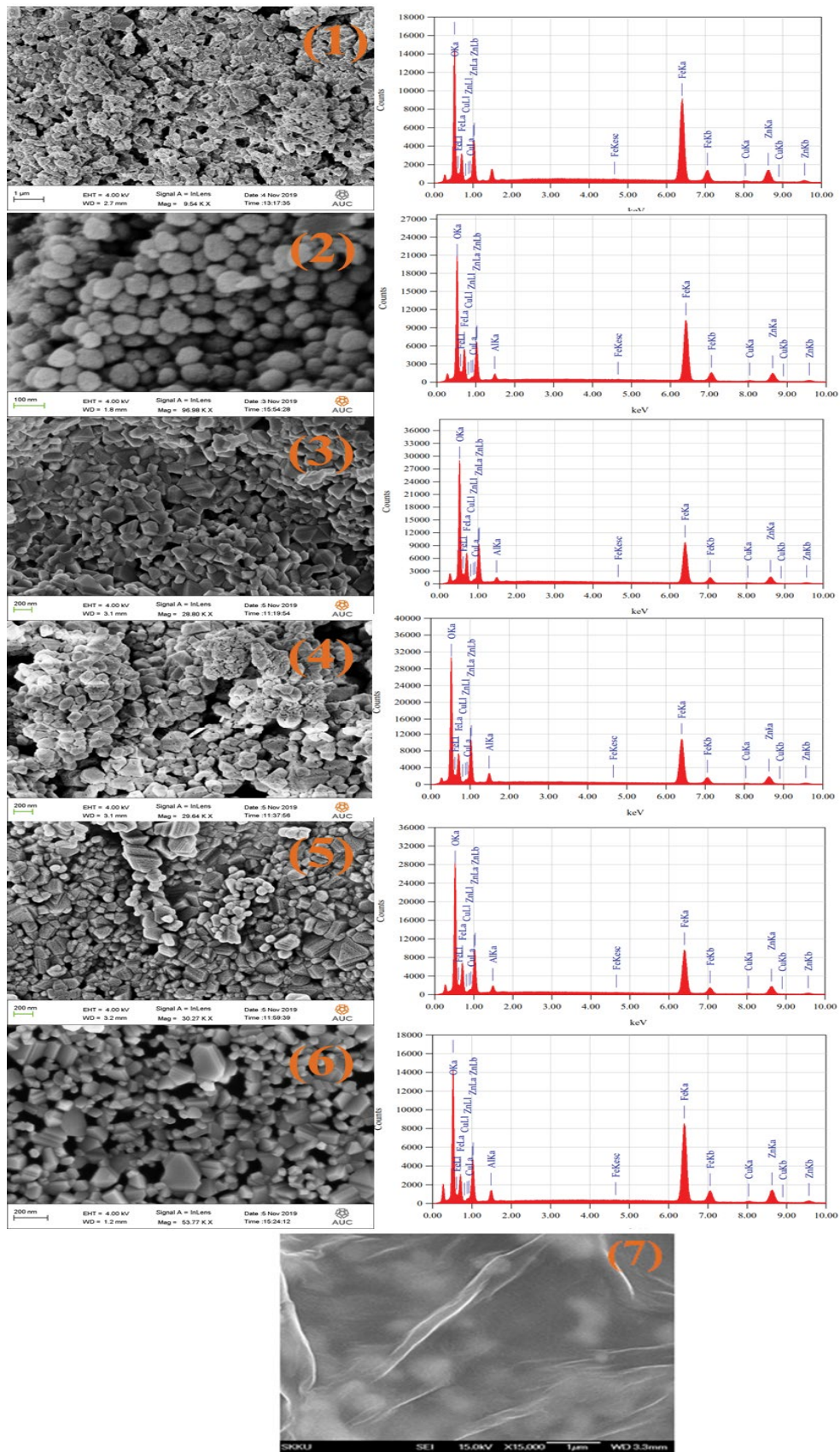
Fig. 6. (1–6) SEM and EDX of $Cu_{0.5}Zn_{0.5}Al_xFe_{2-x}O_4$ nanoparticles and (7) SEM of $Cu_{0.5}Zn_{0.5}Al_{0.03}Fe_{1.97}O_4$/rGO composite.
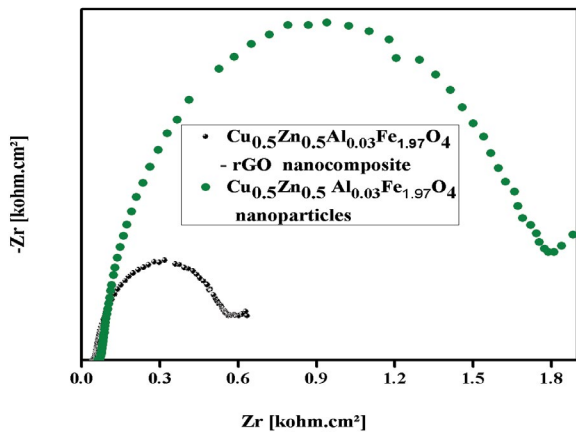
Fig. 7. Nyquist plots of $Cu_{0.5}Zn_{0.5}Al_{0.03}Fe_{1.97}O_4$ and $Cu_{0.5}Zn_{0.5}Al_{0.03}Fe_{1.97}O_4$/rGO composite.

photocatalytic material for the degradation of methylene blue present as an impurity in water. It was due to the rGO sheets that inhibit the recombination of electron-hole pair in the $Ni_{0.65}Zn_{0.35}Fe_2O_4$/rGO nanocomposites. In this work to check the degradation of methylene blue, a dilute solution of MB (5 ppm) was prepared. In this MB solution addition of 0.01 g of $Ni_{0.65}Zn_{0.35}Fe_2O_4$/rGO composites. With the time interval of 5 mins, UV-visible spectra of $Ni_{0.65}Zn_{0.35}Fe_2O_4$/rGO composite was recorded by taking a smaller amount of this solution say (4 mL) followed by centrifugation. From UV visible spectra in Fig. 8, it is evident that methylene blue shows two peaks at 616 and 664 nm. When methylene blue containing $Ni_{0.65}Zn_{0.35}Fe_2O_4$/rGO nanocomposite was irradiated to visible light then peak intensity at 664 nm begins to decrease. While with that of pure $Ni_{0.65}Zn_{0.35}Fe_2O_4$ nanoparticles' decline in peak intensity was not cleared. After some time, the color of methylene blue turned lighter in the case of $Ni_{0.65}Zn_{0.35}Fe_2O_4$/rGO nanocomposite that showed the photocatalytic activity of $Ni_{0.65}Zn_{0.35}Fe_2O_4$/rGO is much greater than that of $Ni_{0.65}Zn_{0.35}Fe_2O_4$ nanoparticles. Therefore, we can say that the $Ni_{0.65}Zn_{0.35}Fe_2O_4$/rGO nanocomposite decomposed the methylene blue within a relatively short time as compared to pure $Ni_{0.65}Zn_{0.35}Fe_2O_4$ nanoparticles.
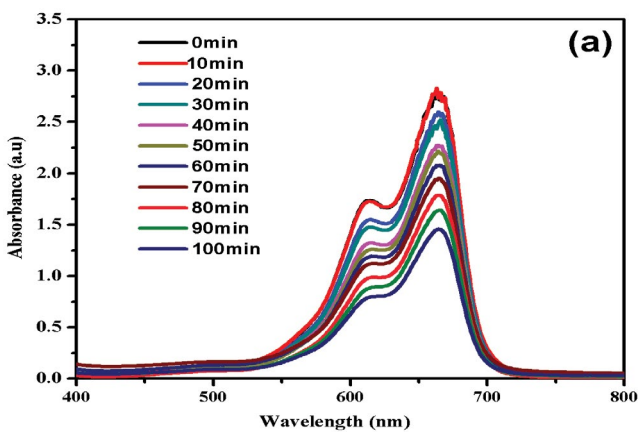
$Cu_{0.5}Zn_{0.5}Al_{0.03}Fe_{1.97}O_4$ nanoparticles exhibited 44.44% degradation whereas $Cu_{0.5}Zn_{0.5}Al_{0.03}Fe_{1.97}O_4$/rGO composited exhibited 90% degradation under solar light irradiation for a given timeline. Furthermore, bare photocatalyst degraded methylene blue with 0.003 min t^{-1} and rGO based nano-composite with 0.005 min t^{-1} rate constant. The kinetics of the overall degradation process is given in Fig. 9.

The cyclic stability and reusability of $Cu_{0.5}Zn_{0.5}Al_{0.03}Fe_{1.97}O_4$/rGO composite were also tested and given in Fig. 10. It was observed that by applying five cycles, 10% degradation efficiency was lost, this made it a suitable candidate for the degradation of organic pollutants.

The morphological and structural stability of photocatalyst was also tested by SEM and XRD analysis after the photocatalytic degradation reaction. Fig. 11 shows the SEM and XRD pattern of $Cu_{0.5}Zn_{0.5}Al_{0.03}Fe_{1.97}O_4$ nanoparticles. It was found that photocatalyst was highly morphologically and structurally stable after the photocatalytic degradation process.

Degradation of methylene blue by photocatalytic activity can be explained in the following steps and schematically is shown in Fig. 12.

- *Step 1*: when $Ni_{0.65}Zn_{0.35}Fe_2O_4$ is exposed to solar light, this will result in the generation of e^-–h^+ pair [36].

$$Ni_{0.65}Zn_{0.35}Fe_2O_4 + hv \rightarrow Cu_{0.5}Zn_{0.5}Al_xFe_{2-x}O_4 + e^-CB + h^+_{vb} \quad (4)$$
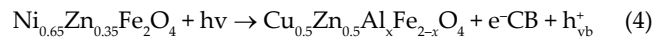
- *Step 2*: The electron-hole pair that generated in step one can be recombined if we used $Ni_{0.65}Zn_{0.35}Fe_2O_4$ alone as a photocatalyst to avoid it we used its composite with rGO. rGO has a high capacity for charge separation so it prevents the recombination of electron-hole pair.
- *Step 3*: The photogenerated electrons from the conduction band reacts with O_2 and form $O_2^{\bullet-}$. This $O_2^{\bullet-}$ leads to the degradation of methylene blue.

$$e^-CB + O_2 \rightarrow O_2^{\bullet-} \quad (5)$$

- *Step 4*: Holes present in the valance band oxidized the hydroxyl ions leading to the formation of $OH^{\bullet}$ radicals that degraded the methylene blue.
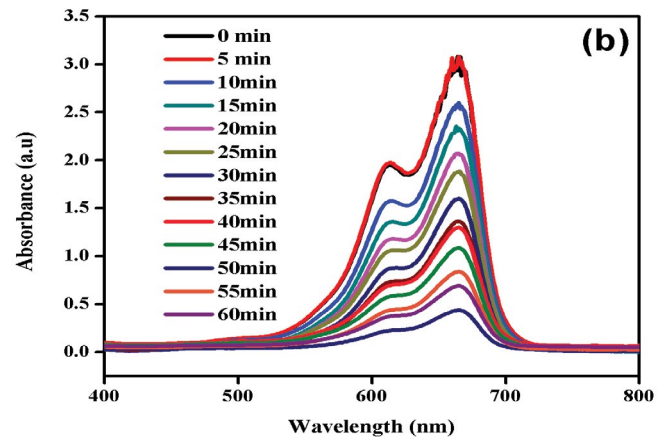

Fig. 8. (a) Degradation of "MB" in the presence of ferrite nanoparticles and (b) Degradation of "MB" in the presence of ferrite nano-composites.
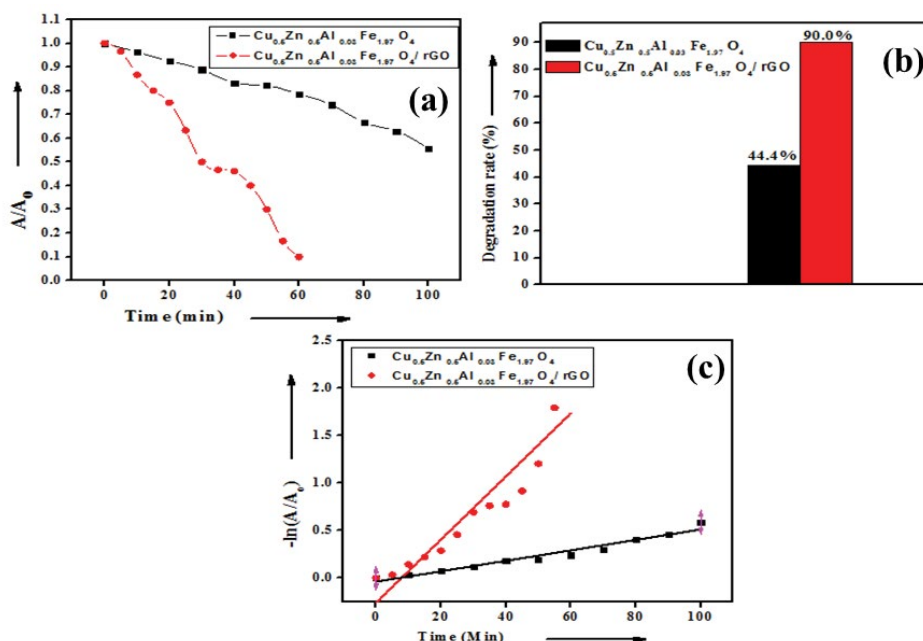
Fig. 9. (a) A/A_0 plot, (b) percent degradation, and (c) $-\ln(A/A_0)$ vs. time plot.
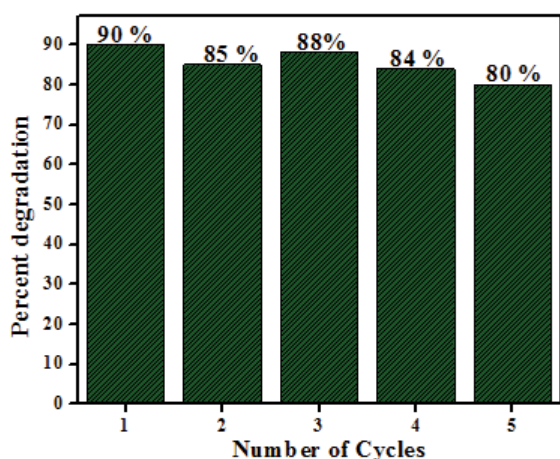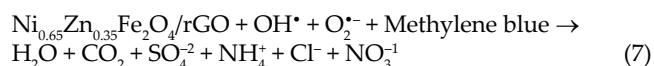

Fig. 10. Cyclic stability of $Cu_{0.5}Zn_{0.5}Al_{0.03}Fe_{1.97}O_4$/rGO composite for degradation of methylene blue.

$$h_{vb}^+ + OH^- \rightarrow OH^\bullet \tag{6}$$

- *Step 5*: Finally, the methylene blue dye was degraded to colorless compounds such as CO_2, H_2O, and SO_4^{-2}, NH_4^+, NO_3^{-1}, and Cl^{-1}.

$$Ni_{0.65}Zn_{0.35}Fe_2O_4/rGO + OH^\bullet + O_2^{\bullet-} + \text{Methylene blue} \rightarrow$$
$$H_2O + CO_2 + SO_4^{-2} + NH_4^+ + Cl^- + NO_3^{-1} \tag{7}$$

4. Conclusion

Magnetically separable $Cu_{0.5}Zn_{0.5}Al_xFe_{2-x}O_4$ nanoparticles were fabricated successfully by the cheap synthetic route. XRD confirmed the successful doping of Al^{3+} at the octahedral sites of spinel $Cu_{0.5}Zn_{0.5}Fe_2O_4$ ferrite nanoparticles. The characterization of The $Cu_{0.5}Zn_{0.5}Al_xFe_{2-x}O_4$ nanoparticles and their nano-heterostructures with rGO was carried out by a variety of characterization techniques such as XRD,

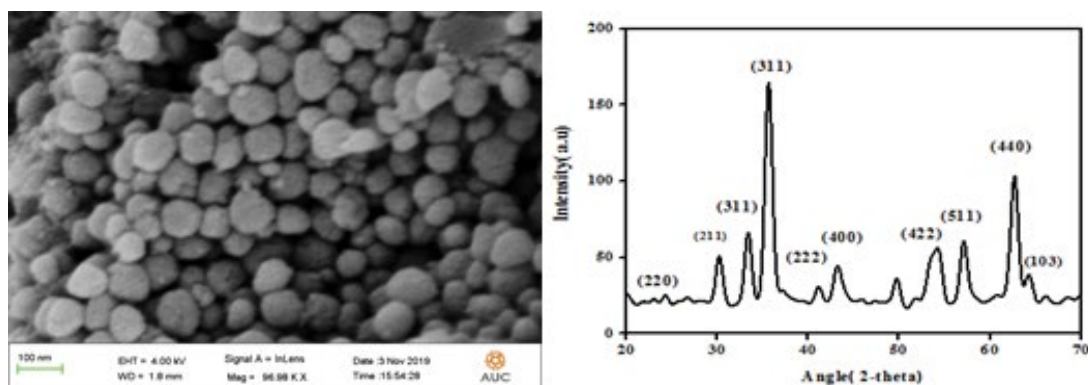Fig. 11. SEM and XRD pattern of typical $Cu_{0.5}Zn_{0.5}Al_{0.03}Fe_{1.97}O_4$ nanoparticles after photocatalytic degradation experiment.
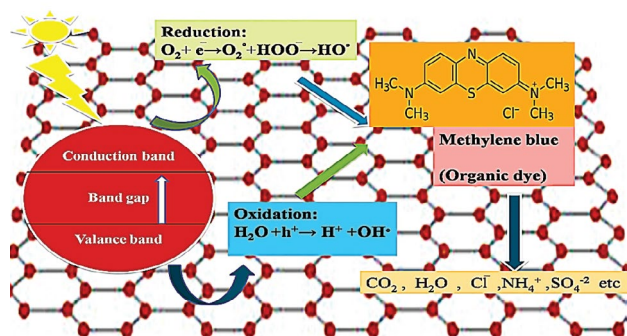
Fig. 12. Photocatalysis of $Cu_{0.5}Zn_{0.5}Al_{0.03}Fe_{1.97}O_4$/rGO nano-composite.

UV-visible spectroscopy, SEM/EDX, and EIS. The photocatalytic degradation of methylene blue in the presence of prepared Al^{3+} doped spinel ferrite ($Cu_{0.5}Zn_{0.5}Fe_2O_4$) nanoparticles and their composite/nano-heterostructures with rGO was carried out under visible light irradiation. The photocatalytic results revealed that bare nanoparticles' photocatalytic activity was much less as compared to $Ni_{0.65}Zn_{0.35}Fe_2O_4$/rGO nano-heterostructures. It was the rGO, that enhanced the photocatalytic activity of ferrite nanoparticles.

Acknowledgments

References

[1] N.-u. Ain, W. Shaheen, B. Bashir, N.M. Abdelsalam, M.F. Warsi, M.A. Khan, M. Shahid, Electrical, magnetic and photoelectrochemical activity of rGO/MgFe$_2$O$_4$ nanocomposites under visible light irradiation, Ceram. Int., 42 (2016) 12401–12408.
[2] C. Han, N. Zhang, Y.-J. Xu, Structural diversity of graphene materials and their multifarious roles in heterogeneous photocatalysis, Nano Today, 11 (2016) 351–372.
[3] D. Chen, Z. Jiang, J. Geng, Q. Wang, D. Yang, Carbon and nitrogen Co-doped TiO$_2$ with enhanced visible-light photocatalytic activity, Appl. Mater. Interfaces, 46 (2007) 2741–2746.
[4] J. Tang, Z. Zou, J. Ye, Efficient photocatalytic decomposition of organic contaminants over CaBi$_2$O$_4$ under visible-light irradiation, Angew. Chem., 43 (2004) 4462–4466.
[5] Y. Fu, P. Xiong, H. Chen, X. Sun, X. Wang, High photocatalytic activity of magnetically separable manganese ferrite graphene heteroarchitectures, Ind. Eng., 51 (2012) 725–731.
[6] S. Nazim, T. Kousar, M. Shahid, M.A. Khan, G. Nasar, M. Sher, M.F. Warsi, New graphene-Co$_x$Zn$_{1-x}$Fe$_2$O$_4$ nano-heterostructures: magnetically separable visible light photocatalytic materials, Ceram. Int., 42 (2016) 7647–7654.
[7] X. Zeng, W. Zhang, X. Xiao, C. Wan, H. Wang, Interfacial charge transfer and mechanisms of enhanced photocatalysis of an anatase TiO$_2$(001)-MoS$_2$-graphene nanocomposite: a first-principles investigation, Comput. Mater., 126 (2017) 43–51.
[8] S. Yousaf, T. Kousar, M.B. Taj, P.O. Agboola, I. Shakir, M.F. Warsi, Synthesis and characterization of double heterojunction-graphene nano-hybrids for photocatalytic applications, Ceram. Int., 45 (2019) 17806–17817.
[9] X. Chen, Y. Dai, J. Guo, T. Liu, X. Wang, Novel magnetically separable reduced graphene oxide (RGO)/ZnFe$_2$O$_4$/Ag$_3$PO$_4$ nanocomposites for enhanced photocatalytic performance toward 2,4-dichlorophenol under visible light, Ind. Eng., 55 (2016) 568–578.
[10] A. Rasheed, M. Mahmood, U. Ali, M. Shahid, I. Shakir, S. Haider, M.A. Khan, M.F. Warsi, Zr$_x$Co$_{0.8-x}$Ni$_{0.2-x}$Fe$_2$O$_4$-graphene nanocomposite for enhanced structural, dielectric and visible light photocatalytic applications, Ceram. Int., 42 (2016) 15747–15755.
[11] A. Iftikhar, S. Yousaf, F.A. Ahmed Ali, S. Haider, S. Ud-Din Khan, I. Shakir, F. Iqbal, M.F. Warsi, Erbium-substituted Ni$_{0.4}$Co$_{0.6}$Fe$_2$O$_4$ ferrite nanoparticles and their hybrids with reduced graphene oxide as magnetically separable powder photocatalyst, Ceram. Int., 46 (2020) 1203–1210.
[12] L. Zhang, J. Lian, L. Wu, Z. Duan, J. Jiang, L. Zhao, Synthesis of a thin-layer MnO$_2$ nanosheet-coated Fe$_3$O$_4$ nanocomposite as a magnetically separable photocatalyst, ACS Appl. Mater. Interfaces, 30 (2014) 7006–7013.
[13] Y. Fu, H. Chen, X. Sun, X. Wang, Combination of cobalt ferrite and graphene: high-performance and recyclable visible-light photocatalysis, Appl. Catal., B, 111–112 (2012) 280–287.
[14] H. Javed, A. Rehman, S. Mussadiq, M. Shahid, M. Khan, I. Shakir, P. Agboola, M. Aboud, M. Warsi, Reduced graphene oxide-spinel ferrite nano-hybrids as magnetically separable and recyclable visible light driven photocatalyst, Synth. Met., 254 (2019) 1–9.
[15] A. Shabbir, S. Ajmal, M. Shahid, I. Shakir, P. Agboola, M. Warsi, Zirconium substituted spinel nano-ferrite Mg$_{0.2}$Co$_{0.8}$Fe$_2$O$_4$ particles and their hybrids with reduced graphene oxide for photocatalytic and other potential applications, Ceram. Int., 45 (2019) 16121–16129.
[16] M. Mahmood, M.A. Yousuf, M.M. Baig, M. Imran, M. Suleman, M. Shahid, M.A. Khan, M.F. Warsi, Spinel ferrite magnetic nanostructures at the surface of graphene sheets for visible light photocatalysis applications, Physica B, 550 (2018) 317–323.
[17] O. Raina, R. Manimekalai, Photocatalysis of cobalt zinc ferrite nanorods under solar light, Res. Chem. Intermed., 44 (2018) 5941–5951.
[18] G. Fan, J. Tong, F. Li, Visible-light-induced photocatalyst based on cobalt-doped zinc ferrite nanocrystals, Ind. Eng., 51 (2012) 13639–13647.
[19] W. Wang, N. Li, K. Hong, H. Guo, R. Ding, Z. Xia, Z-scheme recyclable photocatalysts based on flower-like nickel zinc ferrite nanoparticles/ZnO nanorods: enhanced activity under UV and visible irradiation, J. Alloys Compd., 777 (2019) 1108–1114.
[20] S. Akbari, S.M. Masoudpanah, S.M. Mirkazemi, N. Aliyan, PVA assisted coprecipitation synthesis and characterization of MgFe$_2$O$_4$ nanoparticles, Ceram. Int., 43 (2017) 6263–6267.
[21] L. Sun, B. Fugetsu, Mass production of graphene oxide from expanded graphite, Mater. Lett., 109 (2013) 207–210.
[22] N. Rezlescu, E. Rezlescu, C. Pasnicu, M.L. Craus, Comparison of the effects of TiO$_2$-GeO$_2$ and R$_2$O$_3$ substitutions in a high frequency nickel-zinc ferrite, J. Magn. Magn. Mater., 136 (1994) 319–326.
[23] M.A. Ahmed, E. Ateia, L.M. Salah, A.A. El-Gamal, Structural and electrical studies on La^{3+} substituted Ni–Zn ferrites, Mater. Chem. Phys., 92 (2005) 310–321.
[24] L. Stobinski, B. Lesiak, A. Malolepszy, M. Mazurkiewicz, B. Mierzwa, J. Zemek, P. Jiricek, I. Bieloshapka, Graphene oxide and reduced graphene oxide studied by the XRD, TEM and electron spectroscopy methods, J. Electron. Spectro., 195 (2014) 145–154.
[25] G.R. Kumar, K.V. Kumar, Y.C. Venudhar, Synthesis, structural and magnetic properties of copper substituted nickel ferrites by sol-gel method, Mater. Sci. Appl., 3 (2012) 87–91.
[26] S. Mandal, S. Natarajan, A. Tamilselvi, S. Mayadevi, Photocatalytic and antimicrobial activities of zinc ferrite nanoparticles synthesized through soft chemical route: a magnetically

recyclable catalyst for water/wastewater treatment, J. Environ. Chem. Eng., 4 (2016) 2706–2712.

[27] V. Narayanaswamy, I.M. Obaidat, A.S. Kamzin, S. Latiyan, S. Jain, H. Kumar, C. Srivastava, S. Alaabed, B. Issa, Synthesis of graphene oxide-Fe_3O_4 based nanocomposites using the mechanochemical method and in vitro magnetic hyperthermia, Int. J. Mol. Sci., 20 (2019) 3368.

[28] A. Yousuf, M. Mahmood, N. Al-Khalli, M. Khan, M. Aboud, I. Shakir, M. Warsi, The impact of yttrium cations (Y^{3+}) on structural, spectral and dielectric properties of spinel manganese ferrite nanoparticles, Ceram. Int., 45 (2019) 10936–10942.

[29] Z.A. Gilani, M.F. Warsi, M.A. Khan, I. Shakir, M. Shahid, M.N. Anjum, Impacts of neodymium on structural, spectral and dielectric properties of $LiNi_{0.5}Fe_2O_4$ nanocrystalline ferrites fabricated via micro-emulsion technique, Physica E, 73 (2015) 169–174.

[30] S. Yousaf, S. Zulfiqar, M.N. Shahi, M.F. Warsi, N.F. Al-Khalli, M.F. Aly Aboud, I. Shakir, Tuning the structural, optical and electrical properties of NiO nanoparticles prepared by wet chemical route, Ceram. Int., 46 (2020) 3750–3758.

[31] D. Zhang, Y. Zhang, L. Zheng, Y. Zhan, L. He, Graphene oxide/poly-l-lysine assembled layer for adhesion and electrochemical impedance detection of leukemia K562 cancercells, Biosens. Bioelectron., 42 (2013) 112–118.

[32] S. Zhai, S. Gong, J. Jiang, S. Dong, J. Li, Assembly of multilayer films containing iron(III)-substituted Dawson-type heteropolyanions and its electrocatalytic properties: cyclic voltammetry, electrochemical impedance spectroscopy and UV-Vis spectrometry, Anal. Chim. Acta, 486 (2003) 85–92.

[33] J. Ma, T. Xue, X. Qin, Sugar-derived carbon/graphene composite materials as electrodes for supercapacitors, Electrochim. Acta, 115 (2014) 566–572.

[34] E. Casbeer, V.K. Sharma, X.-Z. Li, Synthesis and photocatalytic activity of ferrites under visible light: a review, Sep. Purif. Technol., 87 (2012) 1–14.

[35] A. Rasheed, M. Mahmood, U. Ali, M. Shahid, I. Shakir, S. Haider, M.A. Khan, M.F. Warsi, $Zr_xCo_{0.8-x}Ni_{0.2-x}Fe_2O_4$-graphene nanocomposite for enhanced structural, dielectric and visible light photocatalytic applications, Ceram. Int., 42 (2016) 15747–15755.

[36] C. Salameh, J.-P. Nogier, F. Launay, M. Boutros, Dispersion of colloidal TiO_2 nanoparticles on mesoporous materials targeting photocatalysis applications, Catal. Today, 257(Pt 1) (2015) 35–40.